

Molecular interferometric imaging

Ming Zhao, Xuefeng Wang and David D. Nolte*

Department of Physics, Purdue University, 525 Northwestern Avenue, West Lafayette, IN 47907

*Corresponding author: nolte@purdue.edu

Abstract: Common-path in-line shearing interferometry, combined with pixel-array imaging, provides a surface metrology that achieves 15 pm surface height resolution. An eighth-wave thermal oxide on silicon generates a reference wave locked in the condition of phase quadrature for phase-to-intensity conversion that makes surface height or index variations directly detectable by an imaging system. The scaling surface mass sensitivity for the surface metrology application is $S_{\text{scal}} = 7 \text{ fg/mm}$ under 40x magnification with a molecular resolution of approximately 12 IgG molecules within a pixel, limited by the surface roughness of the substrate. When applied to reverse-phase immunoassays in an antibody microarray format under 7x magnification, the current limit of detection is 10 ng/ml for 1 hour incubation, limited by biological and chemical variability. The biosensor is compatible with real-time binding measurements under active flow conditions with a binding dynamic range per well of 10^3 and a mass sensitivity of 2 pg/mm^2 .

©2008 Optical Society of America

OCIS codes: (170.1470) Blood or tissue constituent monitoring; (170.0110) Imaging systems; (170.0180) Microscopy; (110.3175) Interferometric imaging.

References and Links

1. N. L. Anderson and N. G. Anderson, "The human plasma proteome - History, character, and diagnostic prospects," *Mol. Cell. Proteomics* **1**, 845-867 (2002).
2. G. Gauglitz, "Direct optical sensors: principles and selected applications," *Anal. Bioanal. Chem.* **381**, 141-155 (2005).
3. J. Homola, "Present and future of surface plasmon resonance biosensors," *Anal. Bioanal. Chem.* **377**, 528-539 (2003).
4. B. Cunningham, P. Li, and J. Pepper, "Colorimetric resonant reflection as a direct biochemical assay technique," *Sens. Actuators B* **81**, 316-328 (2002).
5. M. Armani, A. P. Kulkarni, S. E. Fraser, R. C. Flagen, and K. J. Vahala, "Label-free, single-molecule detection with optical microcavities," *Science* **317**, 783-787 (2007).
6. M. M. Varma, D. D. Nolte, H. D. Inerowicz, and F. E. Regnier, "Spinning-disk self-referencing interferometry of antigen-antibody recognition," *Opt. Lett.* **29**, 950-952 (2004).
7. D. D. Nolte and M. Zhao, "Scaling mass sensitivity of the BioCD at 0.25 pg/mm," in *Smart Medical and Biomedical Sensor Technology IV*, B. M. Cullum and J. Chance Carter, eds., Proc. SPIE **6380** 63800J (2006).
8. M. M. Varma, H. D. Inerowicz, F. E. Regnier, and D. D. Nolte, "High-speed label-free detection by spinning-disk micro-interferometry," *Biosens. Bioelectron.* **19**, 1371-1376 (2004).
9. L. Peng, M. M. Varma, W. Cho, F. E. Regnier, and D. D. Nolte, "Adaptive interferometry of protein on a BioCD," *Appl. Opt.* **46**, 5384-5395 (2007).
10. M. Zhao, W. R. Cho, F. Regnier, and D. Nolte, "Differential phase-contrast BioCD biosensor," *Appl. Opt.* **46**, 6196-6209 (2007).
11. X. F. Wang, M. Zhao, and D. D. Nolte, "Common-path interferometric detection of protein monolayer on the BioCD," *Appl. Opt.* **46**, 7836-7849 (2007).
12. M. Bras, V. Dugas, F. Bessueille, J. P. Cloared, J. R. Martin, M. Cabrera, J. P. Chauvet, E. Souteyrand, and M. Garrigues, "Optimization of a silicon/silicon dioxide substrate for fluorescence DNA microarray," *Biosens. and Bioelectron.* **20**, 797-806 (2004).
13. T. J. Gao, J. H. Lu, and L. J. Rothberg, "Biomolecular sensing using near-null single wavelength arrayed imaging reflectometry," *Anal. Chem.* **78**, 6622-6627 (2006).
14. K. Johansen, H. Arwin, I. Lundstrom, and B. Liedberg, "Imaging surface plasmon resonance sensor based on multiple wavelengths: Sensitivity considerations," *Rev. Sci. Instrum.* **71**, 3530-3538 (2000).

15. J. Dyson, "Common-Path Interferometer For Testing Purposes," *J. Opt. Soc. Am.* **47**, 386-390 (1957).
 16. P. Hariharan, *Optical Interferometry* (Elsevier, 2003).
 17. V. Kiessling and L. K. Tamm, "Measuring distances in supported bilayers by fluorescence interference-contrast microscopy: Polymer supports and SNARE proteins," *Biophys. J.* **84**, 408-418 (2003).
 18. V. Jacobsen, P. Stoller, C. Brunner, V. Vogel, and V. Sandoghdar, "Interferometric optical detection and tracking of very small gold nanoparticles at a water-glass interface," *Opt. Express*
 19. O. S. Heavens, *Optical Properties of Thin Solid Films* (Dover, 1991).
-

1. Introduction

The human blood proteome contains over 10,000 proteins, many of which relate to the health and disease of individuals [1]. To detect large numbers of these proteins in a patient sample requires highly-multiplexed label-free methods that detect the protein molecules directly. Label-free optical detection, through the interaction of molecular polarizability with light, is being pursued using many different phenomena [2], the principal being evanescent wave approaches such as surface plasmon resonance [3], waveguides [4], and ring micro-resonators [5]. The use of high-Q ring resonators has recently enabled the detection of single molecules adjacent to the edge of a micro-disc. However, many of these approaches require either extensive sample fabrication, tight tolerance on resonance conditions, or large areas, any of which do not naturally lend themselves to low-cost highly-multiplexed protein arrays. In contrast, high-speed laser scanning of proteins using common-path interferometry in spinning-disc BioCD formats [6] detects proteins across broad-area surfaces, with capacity to scan over 25,000 protein spots with scaling mass sensitivity of 0.25 pg/mm in minutes [7]. Spinning-disc interferometry has been demonstrated in several common-path configurations, including micro-diffraction [8], adaptive optical [9], phase contrast [10] and in-line [11]. The conditions that maximize phase-contrast interferometry are also the same used in fluorescence interference imaging [12], but interferometry requires no labels.

Although laser scanning has the advantage of high-speed access to arrays of protein spots across broad areas, it is limited by serial data acquisition. On the other hand, a parallel multiplex advantage can be attained through the use of direct imaging and CCD pixel arrays that acquire many modes simultaneously. This approach has been used by imaging ellipsometry and imaging surface plasmon resonance to detect protein spots directly on surfaces [13, 14], but requires the use of non-normal-incident light and polarization control. As a simple and inexpensive alternative, we present an interferometric imaging approach for the direct detection of proteins that combines common-path [15] and shearing [16] interferometry. This approach can be applied in a conventional reflective light microscope using conventional light sources and Koehler illumination and color filters. No off-angle illumination nor polarization control is needed. Common-path interferometry has been applied to various applications, including maximizing surface electric field to enhance fluorescence [17], and interference detection of the scattered field from gold nanoparticles [18]. However, due to its limited non-resonant optical interaction with molecular dipole moments, common-path interferometry has not been applied for direct label-free detection of biomolecules, which produce much smaller interactions with the probe beam compared to gold nanoparticles. In this work, we apply common-path interferometry in an in-line quadrature configuration with an eighth-wave oxide on silicon to establish phase quadrature interference that maximizes interferometry sensitivity, and uses shearing interferometry to achieve surface-roughness-limited detection sensitivity of biomolecules. When it is applied as a surface metrology, this approach is shot-noise limited and has a resolution of 15 pm or about 12 antibody molecules within a pixel. When used to measure real-time binding, it has a mass sensitivity of 2 pg/mm² comparable to conventional SPR sensitivities, but can be applied across broad areas without the need to maintain or track resonance conditions.

In the next section, we present the theoretical conditions for in-line phase quadrature interferometry, and calculate and measure the conversion coefficient of protein-to-intensity

modulation when a thermal oxide on silicon is used as the substrate. The scaling sensitivity for label-free mass detection is discussed in terms of temporal and spatial averaging of the mass binding. The optical detection system is described in Section 3, including details of protein immobilization on the oxide and sample incubation protocols. The demonstration of the shot-noise-limited surface metrology is presented in Section 4, followed by performance in idealized assays and practical assays in Sections 5 and 6, respectively. These assays use off-line incubation and image the protein bound to the target spots after the surface is re-dried. However, the imaging approach also lends itself to the measurement of real-time binding kinetics under on-line wet chemistry that does not require a dismount nor dry-down to read, which we describe in Section 7.

2. Interferometric biolayer reflectometry

Interferometry converts phase changes into intensity changes for photon detection by combining a phase-modulated signal wave with a reference wave that has a relative phase set to $\pi/2$, a condition called phase quadrature. For instance, biolayers bound on simple surfaces modify the phase of a reflected wave, but do not significantly change the reflected amplitude. To convert the biolayer-induced phase to a detectable intensity requires a reference wave that is phase-locked to quadrature to make it insensitive to mechanical vibrations. A simple common-path structure that accomplishes this is shown in Fig. 1. An eighth-wave-thick thermal oxide on silicon provides a reference wave in the phase quadrature condition from the reflection of the partial wave off the lower boundary between the oxide and the silicon. A biolayer on the top surface induces a phase shift proportional to the $n_p h_p$ product (where n_p is the refractive index and h_p is the layer thickness) that is converted into an intensity shift by the interference between the first and the second reflection.

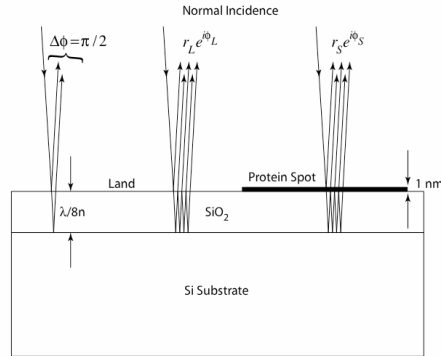


Fig. 1 Thermal oxide layer on silicon for an in-line common-path interferometric condition that converts phase to intensity through the phase quadrature condition set by an eighth-wave thickness.

Light reflected from the dielectric structure from the land (the area not covered by the biolayer) has a complex reflection coefficient $r_L e^{i\phi_L}$. The thin biolayer is treated as an additional dielectric film and the reflection coefficient is calculated by the transfer matrix method. For a thin biolayer ($h_p \ll \lambda$) the difference of the reflection coefficients between the land and the spot is given by [11]

$$\Delta(r e^{i\phi}) = i \frac{4\pi}{\lambda} n h_p \left(r_L e^{i\phi_L} + \frac{(r_p - r_L e^{i\phi_L})(1 - r_p r_L e^{i\phi_L})}{(1 - r_p^2)} \right) \quad (1)$$

where $n_p h_p$ is the index-height product for the biolayer, r_p is the reflection coefficient of the air-protein interface, and λ is the free-space wavelength. When the phase reflected from the land is $\phi_L = (2N - 1)\pi / 2$, the reflected amplitude change is an extremum and is directly detectable by a photodetector. This condition occurs near the eighth-wave quadrature thickness of the oxide layer. The exact thickness for this condition is between an eighth-wave and a quarter-wave for reasons associated with the field strength at the top boundary, which is explained in detail in Ref. [11]. The change in reflected intensity is

$$\Delta I(x, y) = C(\lambda, d) (g^2(x, y) \otimes h(x, y)) \quad (2)$$

where g is the normalized point-spread function of the imaging system, the square of which is convolved with the protein height function $h(x, y)$. The coefficient $C(\lambda, d)$ that gives the conversion from biolayer height to intensity is

$$C(\lambda, d) \approx \frac{8\pi n}{\lambda} \operatorname{Im} \left(\frac{(r_p - r_L e^{i\phi_L})(1 - r_p r_L e^{i\phi_L})}{1 - r_p^2} \right) \quad (3)$$

where the wavelength and the oxide thickness are contained in the dependences of the amplitude r_L and the phase ϕ_L , which are calculated using a transfer matrix approach [19].

The conversion factor $C(\lambda, d)$ is plotted in Fig. 2 as a function of oxide thickness for three selected wavelengths of 635 nm, 532 nm and 440 nm using incoherent illumination and 10 nm bandpass filters. The data on the figure are experimental values obtained from printed protein spots on substrates with three different oxide thicknesses of 80 nm, 100 nm and 120 nm. The error in the data are from uncertainties in the height of the printed protein. The maximum conversion from protein height to intensity under quadrature conditions is approximately 2% per nm. Under the conditions that maximize fluorescent interferometric microscopy [17], the protein conversion coefficient for label-free detection actually vanishes. There are two opposite quadrature conditions on each side of the zero-crossing. We work at the higher oxide thickness because protein produces a positive signal, while light scattering causes a negative signal. This makes it possible to differentiate between molecular layers and Rayleigh scattering.

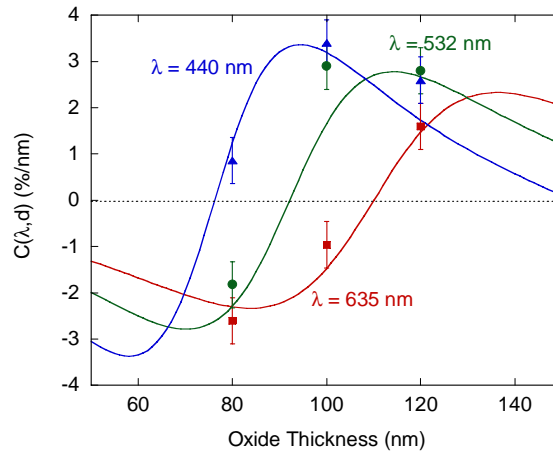


Fig. 2 Theoretical protein conversion coefficient, in percent change in reflectance per nm of protein, as a function of oxide thickness for three wavelengths of 440 nm (blue), 532 nm (green) and 635 nm (red). Data are experimental values measured at the 3 wavelengths and plotted with corresponding color. Error in the data are dominated by uncertainty in the printed protein thickness.

When the photodetector is a CCD array, the detected intensity is

$$I_{ij} = \eta F_{ij} (|r_L|^2 + \Delta I_{ij}) \quad (4)$$

where ij refer to the pixel coordinates, F_{ij} is the photon fluence at the ij^{th} pixel, and η is the CCD conversion from photons to electrons. It is not possible to see the protein patterns, represented by ΔI_{ij} , directly in an image because the variation of F_{ij} is 10% to 20%, while protein contributes only a few percent. The illumination variations therefore overwhelm the protein intensity modulation. Subtracting the average intensity cannot help, because it is the spatial variation in the illumination that masks the protein patterns and not the high background.

To remove the background variation we acquire an image I_{ij} , then laterally shift the substrate (supporting the protein spot) by δ pixel lengths, which keeps the illumination field F_{ij} constant, and acquire a new image $I_{i+\delta,j} = \eta F_{ij} (|r_L|^2 + \Delta I_{i+\delta,j})$. The illumination variability in F_{ij} is removed by taking the normalized difference

$$D_{ij} = 2 \frac{(I_{i+\delta,j} - I_{i,j})}{(I_{i+\delta,j} + I_{i,j})} = 2 \frac{(\eta F_{ij} (|r_L|^2 + \Delta I_{i+\delta,j}) - \eta F_{ij} (|r_L|^2 + \Delta I_{ij}))}{(\eta F_{ij} (|r_L|^2 + \Delta I_{i+\delta,j}) + \eta F_{ij} (|r_L|^2 + \Delta I_{ij}))} \approx C(\lambda, d)(h_{i+\delta,j} - h_{ij}) \quad (5)$$

where h_{ij} is the local surface height. Therefore, the large 10% to 20% variation in the illumination is removed, leaving the spatial modulation caused by the protein. This approach requires isolated protein spots surrounded by highly flat land so that the adjacent land acts as the reference surface for the spots. Included within D_{ij} is residual surface roughness as well as shot noise from the CCD array. Shot noise is reduced by averaging many image acquisitions. Surface roughness is not noise, but can be measured accurately and subtracted under assay conditions because it remains the same from before to after incubation with sample. However, the chemistry of the assay leaves residues that limit the ultimate sensitivity of this technique.

An example of D_{ij} measured under 40x magnification for a single spot of immunoglobulin IgG printed on a di-isocyanate surface on 120 nm oxide is shown in Fig. 3. A single protein spot appears as a dual image, one positive and one negative. The positive is caused by subtracting land on one side from the spot, while the negative is caused by subtracting the spot from land on the other side. The protein spot information is the same for both images, but the land is different. By averaging over both spot images, differences in the land can be partially averaged out. Note that this protein spot has structure caused by moderate dry-down after the spot was printed. A three-dimensional visualization of the spot is shown in Fig. 3(b). The rms surface roughness of the land is 23 pm, while for the smooth region of the spot is 45 pm.

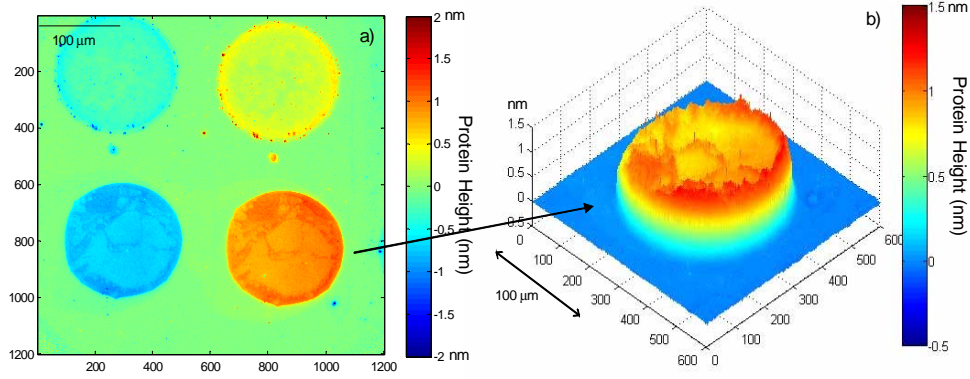


Fig. 3. (a) A plot of D_{ij} after local background normalization of two IgG spots. The red and blue images are of the same protein spot that has been shifted laterally. (b) 3D visualization of the lower protein spot. The lateral imaging resolution is $0.4 \mu\text{m}$ and vertical resolution is 23 pm , limited by surface roughness.

The surface mass sensitivity of any label-free mass-detection technique is a function of averaging. This includes averaging over time with multiple image acquisitions, in which the shot noise of each pixel is reduced, and averaging over space with multiple pixels averaged within a single protein spot. For N image acquisitions and M pixels, the minimum resolvable height is

$$\begin{aligned} \Delta h_{\min}^2 &= h_{\text{pixel}}^2 \left(\frac{1}{N} + \frac{1}{N_{\max}} \right) \left(\frac{1}{M} + \frac{1}{M_{\max}} \right) \\ &= h_{\text{pixel}}^2 \frac{(N_{\max} + N)(M_{\max} + M)}{NMN_{\max}M_{\max}} \end{aligned} \quad (6)$$

where h_{pixel} is the shot-noise-limited height resolution of a single pixel for a single acquisition. N_{\max} is the number of image acquisitions above which the data are limited by the roughness of the land. M_{\max} is the number of pixels averaged above which the data are limited by spatial inhomogeneities of the land or spot. In the scaling range for $M < M_{\max}$, the scaling mass sensitivity is defined by

$$S_{\text{scal}} = \rho h_{\text{pixel}} \sqrt{\frac{a_{\text{pixel}}}{N_{\max}}} \quad (7)$$

where a_{pixel} is the resolved area of a pixel, and ρ is the protein density. The scaling sensitivity has units of mass per root-area, or mass per length, and depends inversely on magnification because of the pixel resolution. Conventional sensitivities used by many mass detection systems use units of mass per area. This is not an intrinsic property of the detection, because it depends on the area over which the data are averaged, but it can be obtained from the scaling sensitivity S_{scal} by dividing the scaling sensitivity by the square root of the total measurement area

$$S_{\text{mm}^2} = \rho h_{\text{pixel}} \sqrt{\frac{a_{\text{pixel}}}{A_{\text{Tot}} N_{\max}}} = \rho \frac{h_{\text{pixel}}}{\sqrt{MN_{\max}}} = \rho h_{\min} \quad (8)$$

In the following sections we quote values for the scaling sensitivity. However, in the final section on the reverse-phase assays, we quote the conventional sensitivity to compare with other mass detection techniques.

In this paper, we consider three levels of sensitivity for molecular interferometric imaging. The first is the shot noise limit, which is the fundamental metrology limit for the technique, which measures existing surface topology, including both protein and surface roughness. This shot-noise sensitivity is appropriate for metrology applications, but cannot be used for assay sensitivities. The second sensitivity is an idealized sensitivity that includes substrate dismount (as it would to be incubated), remount and data registration to find the height change for each pixel, but no chemistry. This sets the system sensitivity in the absence of chemical effects or residues. The third sensitivity is under full assay chemistry and represents the actual performance of our current system. This third sensitivity is not fundamental, because surface chemistry and residues can be improved, with the idealized sensitivity as the limiting value.

3. Optical system and protein protocols

We use a reflective microscope (Leica DMR) coupled to a 12-bit CCD camera (Qimaging 4000R 2048x2048 7.4 μm pixel) to image the sample and acquire the data. We use two different light sources. One is a 10 mW 630 nm LED (eLED.com) with a bandwidth of 30 nm. The second is an Oriel model 66187 halogen lamp with 10 nm or 30 nm band-pass filters at wavelengths of 635 nm, 532 nm and 440 nm. The red LED was used for the assays, while the incoherent light source with 30 nm bandpass filter at 635 nm wavelength was used for the scaling studies. Light is directed into the microscope and focused onto the sample by microscope objectives with 7x, 20x or 40x magnification. The corresponding pixel resolutions are 2.2 μm , 0.72 μm and 0.36 μm , respectively. The Airy diffraction limit at 635 nm is 0.39 μm , which is similar to the pixel resolution at 40x magnification. The reflected light is collected by the same objective, and imaged onto the CCD camera, which captures the image to a computer.

The substrates we used were 100 mm diameter silicon wafers with 120 nm silicon dioxide. A wafer was first plasma cleaned, then a hydrophobic barrier was deposited on top of the wafer using a commercial pad printer that separated the disc into 84 or 96 independent wells. The surface was functionalized by vapor deposition with aminopropaldimethyl ethoxy silane (APDMES) that binds protein covalently through an isocyanate cross-linker. The disc was printed by a piezoelectric inkjet protein printer (Scienion Inc., distributed by BioDot) with 300 pL of protein solution, which resulted in 100 μm diameter protein spots. The printed protein concentration was 75 $\mu\text{g}/\text{mL}$ in pH 7.4 10 mM phosphate-buffered saline (PBS).

4. Shot-noise limited detection

The photon transfer curve of the QImaging CCD camera exhibits shot-noise performance for 12-bit A/D units (ADU) larger than 100. One ADU corresponds to about 10 electrons for a full-well depth of 40,000 electrons. The read-out noise of the CCD camera is also about 10 electrons. Therefore, we operate the CCD close to full well and perform frame (N) averaging until we approach the roughness limit for $N > N_{\text{max}}$. The surface height profile obtained by shearing interferometry is a difference surface height profile in which the protein spot is referenced against its adjacent land. Therefore, the roughness of the land contributes to the uncertainty of the protein height measurements.

To study the scaling as a function of N (for single pixels $M = 1$), the standard deviations of the land and spot are plotted in Fig. 4(a) as a function of the number N of image averages, compared to the measured shot noise of the system. The standard deviation of the measurement σ_{measure} is given by

$$\sigma_{\text{measure}}^2 = \sigma_{\text{surface}}^2 + \sigma_{\text{shot-noise}}^2 \quad (9)$$

where σ_{surf} is the rms surface height roughness. For N smaller than 512, the measurements of both spot and land are dominated by shot noise. The shot noise decreases as frame

averaging increases until surface roughness dominates the measurement noise. The roughness of the land and protein spot is calculated from Eq. (9) by subtracting the contribution of the measured photon shot noise from the data fluctuations. This results in 15 pm surface height fluctuations over a 0.4 micron pixel on the land. The roughness of the protein spot is calculated at 40 pm with an average protein height of 0.8 nm. The equivalent number of IgG molecules in each pixel is around 700, and the pixel-to-pixel fluctuation is equivalent to 35 molecules. It is interesting to note that a Poisson distribution of IgG molecules of this number would have a fluctuation of about 25 molecules. Therefore, the fluctuations of the observed protein spot at $N = 4096$ are close to that expected for the small-number limit of molecular detection, but this is a topic for future work.

When the measurement is shot-noise limited, the noise floor is determined by the number of photons collected in a single measurement. Under this condition, averaging over time (N frames) and over space (M pixels) is identical, and there exists a trade-off between sensitivity and integration time/measurement area, as shown in Eq. (6). However, there is a fundamental difference between temporal and spatial averaging, in that temporal averaging is ultimately limited by the random surface roughness, but spatial averaging can average over the random surface roughness if the roughness is a random Gaussian variable. This difference is shown in Fig. 4(b) which shows the standard deviations of the measurements as functions of N frames (for $M = 1$) and M pixels (for $N = 16$). A smooth region on a protein spot was used for the analysis. The horizontal axis is the number of measurements (NM product), and the vertical axis is the standard deviation of the measurements of the protein spot height. When the total number of measurements is below 512, the measurements are in the shot-noise limit, and both temporal and spatial averaging are the same. For larger N the temporal averaging approaches the random surface roughness, while spatial averaging continues to decrease the standard deviation of the protein height measurement by the square root of the number of measurements. If the surface roughness is uncorrelated, spatial averaging can continue to decrease the standard deviation, with a trade-off of larger sensor area. The data in Fig. 4(b) do show a slight deviation from square-root dependence at large M . The scaling mass sensitivity from Eq. (7) for these metrology data in the scaling regime is $S_{scal} = 7 fg / \sqrt{mm^2}$ under 40x magnification with a molecular resolution of approximately 12 IgG molecules within a pixel, limited by the surface roughness of the substrate.

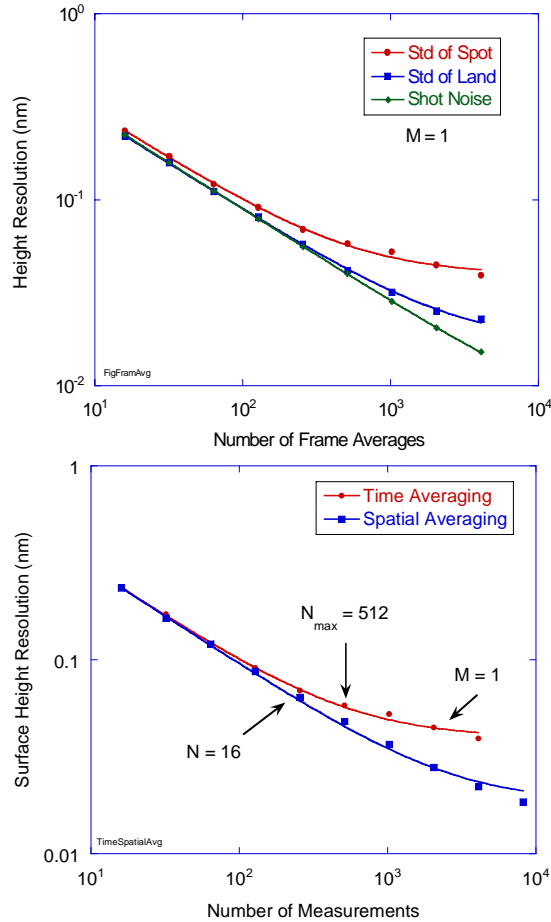


Fig. 4. (a) Height repeatability for single pixels ($M = 1$) as a function of the number of image acquisitions for 40x magnification for a spot, land and shot noise. (b) Comparison of temporal and spatial averaging. The temporal averaging is a function of N at fixed $M = 1$. The spatial averaging is a function of M at fixed $N = 16$. The single-pixel temporal averaging becomes surface-roughness limited at 23 pm for $N > 512$.

5. Idealized assay limits

The sensitivity obtained above is valid for the measurement of a single surface height profile against adjacent land. For an actual assay, the disc needs to be dismantled and incubated with sample solution. To identify the fundamental measurement limits under idealized assay conditions (including off-line handling, but not including residues or chemistry alterations on the substrate surface), we executed the measurement protocol, but not the chemistry protocol, for an assay. In this protocol we image a set of antibody spots using $N = 128$ in a prescan, including a lateral shift with an additional $N = 128$ acquisitions, from which D_{ij}^{pre} is calculated. Then the disc is dismantled, as it would be incubated, and then remounted and remeasured to calculate D_{ij}^{post} . The pre and post images are registered and subtracted to yield the height change for each pixel $\Delta h_{ij} = (D_{ij}^{post} - D_{ij}^{pre}) / C(\lambda, d)$. The results are plotted in Fig. 5 as the root-mean-squared pixel height difference versus magnification, together with the corresponding calculated scaling mass sensitivity defined in Eq. (7). From the figure, the

assay height sensitivity remains almost independent of magnification at 100 pm for each pixel at the different magnifications. Increasing N larger than 128 does not improve this resolution because it is limited by the remounting registration uncertainty that causes a random shift in the convolution between the detection point spread function and the protein height function in Eq. (2). The scaling mass sensitivity under these ideal conditions improves proportionally to the resolution and thus inversely proportionally to the magnification because of the dependence on a_{pixel} in Eq. (7). Under 40x magnification the scaling mass sensitivity is 40 fg/mm for $N = 128$ including the dismount of the substrate but not including chemistry.

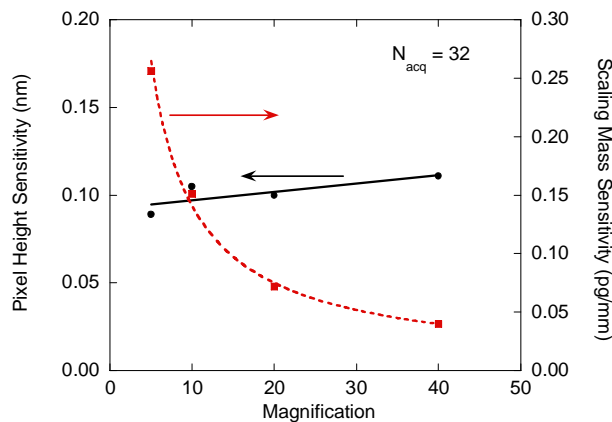


Fig 5. Pixel height resolution and scaling mass sensitivity as a function of magnification for 32 averaged image acquisitions for idealized assay conditions (measurement protocol, but no chemistry). The scaling mass sensitivity depends inversely on the magnification. The best scaling mass sensitivity is 40 fg/mm at 40x.

6. Reverse-phase immunoassays: Practical assay limits

To study the detection limit of a practical assay including chemistry, we performed a reverse-phase immunoassay in which antigen was spotted onto the disc which bound specific antibody out of the sample solution. A 120 nm oxide silicon wafer was used, and it was separated into 84 circular wells by hydrophobic ink printed onto the surface. The disc was coated by vapor-phase deposition of isocyanate chemistry on APDMES on the silica surface. Each well contained 16 2x2 unit cells of mouse and rabbit IgG antigen spots along opposite diagonals for a total of 64 printed antigen spots per well. The sample solutions contained different mixtures of goat anti-mouse IgG, goat anti-rabbit IgG and bovine serum albumin (BSA), each at four concentrations prepared in PBS. The concentrations for anti-mouse were 0, 10 ng/mL, 100 ng/mL and 1 μ g/mL. The concentrations for anti-rabbit were 0, 1 ng/mL, 10 ng/mL and 100 ng/mL. The concentrations for BSA were 0, 10 μ g/mL, 100 μ g/mL and 1mg/mL, acting as a non-specific background protein concentration. Permutations of these concentrations produced 64 different three-component mixtures.

We performed a prescan under 7x magnification of 64 spots per well for 64 of the 84 wells on the disc averaging over $N = 128$ frames. The QImaging CCD camera has a data acquisition rate of 4 fps and an acquisition time for each well of 3 minutes. With a 30 fps CCD camera the full data acquisition can be done in 20 minutes. The disc was dismounted and incubated off-line by filling each well with approximately 30 μ L of sample and letting the disc incubate for one hour using the 64 different mixtures. Figure 6(a) shows the prescan of one unit cell of printed protein spots before incubation, using the 7x objective with 2.2 μ m spatial resolution. This particular well was subsequently incubated with 1 μ g/mL of

anti-mouse. The same unit cell after incubation is shown in Fig. 6(b). The pre- and post-scan images were registered by image cross-correlation, shifted using linear interpolation, and differenced to measure the protein height change for each pixel. The difference image is shown in Fig. 6(c). The specific spots (mouse for this well) increased in height, while the nonspecific spots (rabbit) remained unchanged.

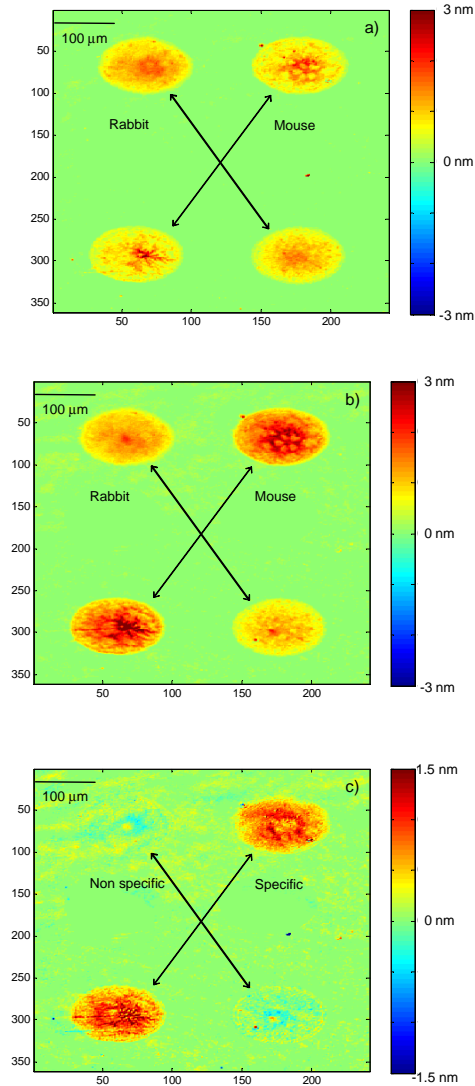


Fig. 6. Reverse immunoassay. (a) Prescan D_{ij} of a 2×2 unit cell. Two rabbit and two mouse spots are printed on opposite diagonals. (b) The same area is scanned again after incubation against $1 \mu\text{g/mL}$ of anti-mouse IgG for 1 hour. The mouse spots increase significantly. (c) Difference of the two scans.

The distributions of the pixel height change for one specific (mouse) and one non-specific (rabbit) spot from this unit cell are shown in Fig. 7. The specific spot (mouse) exhibits an average height change of 0.658 ± 0.004 nm, while the average height of the non-specific spot (rabbit) changes by only 0.037 ± 0.003 nm. Because of the high spatial resolution of the images, each protein spot consists of more than 3000 data points, which yield the small

standard errors of 4 and 3 pm, respectively. The signal-to-noise ratio for this specific unit cell is calculated to be 150:1 at 1 $\mu\text{g/ml}$.

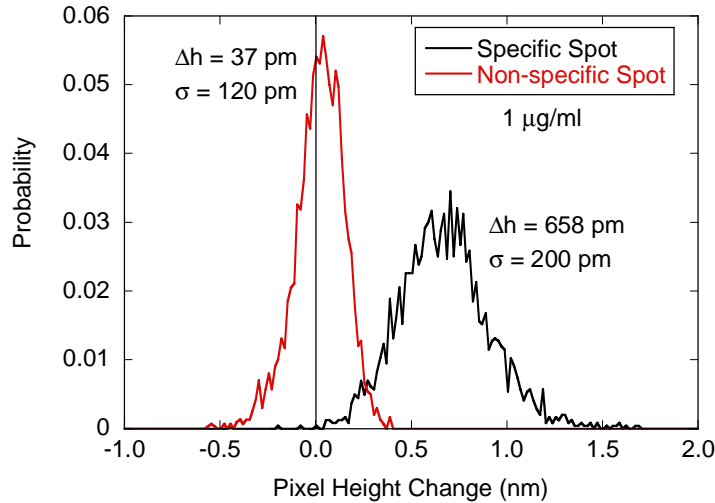


Fig. 7. Histograms of surface height change for one pair of specific and non-specific spots incubated against 1 $\mu\text{g/mL}$ anti-mouse IgG. The signal-to-noise ratio is 150.

Similar analyses were carried out for each of the 64 different mixtures of anti-mouse and anti-rabbit. The spot responses were grouped by analyte concentration, and the average height change for each group is plotted in a dose response shown in Fig. 8. For the specific binding curves of mouse against anti-mouse and rabbit against anti-rabbit, each of the protein height changes were averaged over 512 spots consisting of 32 spots in each of the 16 wells that were incubated with the same concentration for these analytes. Non-specific binding of rabbit against varying concentrations of anti-mouse, and mouse against varying concentrations of anti-rabbit, were obtained by averaging over 128 spots in the 4 wells that were incubated against zero concentration of the specific analyte (at a fixed concentration of the non-specific analyte). For either the specific or non-specific binding, the presence of different concentrations of background BSA did not produce a measurable effect. The specific bindings increased with increasing analyte concentration and were fit to a Langmuir function, while the non-specific binding remained flat around the baseline set by the zero-concentration data.

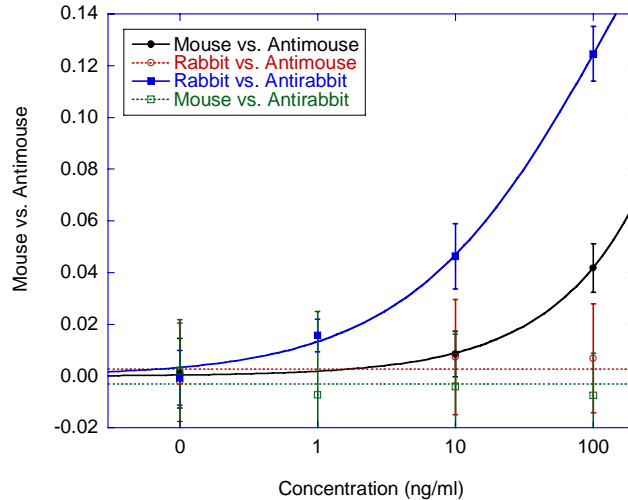


Fig. 8. Concentration response curve for the reverse-phase assay against rabbit and mouse antibodies. Data are averaged over 16 wells. Specific binding increases, while cross-reactivity remains low, as functions of concentration. The limit of detection is approximately 10 ng/ml for rabbit, and 30 ng/ml for mouse. Error bars are dominated by spot-to-spot variability rather than metrology uncertainty.

The error bars in the graph are the standard error set by the statistics of the spots. Although for each protein spot, the error on the measured spot height is only a few picometers with spatial averaging over the pixels, the spot-to-spot differences in the immunoassay response is much larger, at hundreds of picometers, caused by inhomogeneous binding and wash-off. This spot-to-spot variation sets the current detection limit for the practical assay. When averaged over 512 spots, the standard error of the protein response is at the 10 pm level. For the rabbit assay at 10 ng/mL, the average response is separated from the baseline, setting the concentration limit of detection at around 3 ng/mL when averaged over 16 wells, or about 10 ng/mL for a single well. For the mouse assay, the limit of detection is higher at 30 ng/mL for a single well. This is caused by the lower affinity of the reaction that leads to less bound mass during the short incubation time.

7. Dynamic binding

Molecular interferometric imaging is capable of monitoring the real-time binding of antibody to immobilized antigen in a manner analogous to surface plasmon resonance sensors. For this experiment, the disc was separated into 96 wells by deposition of the hydrophobic pad. Wells on the wafer were covered with a 0.17 mm thick microscope glass coverslip attached onto the hydrophobic pad, and one side of the coverslip was connected to a syringe pump (New Era NE500) to introduce sample and control the flow rate. Fluid was drawn into the flow cell by capillary force of the hydrophilic surface of the glass coverslip, and drained from the opposite side of the coverslip by gravity into a reservoir. Channels were made by removing parts of the hydrophobic pad to direct the flow under the coverslip. The protein spots are imaged directly through the cover slip and fluid sample. The flow-cell height was 100 microns, supporting a typical linear fluid velocity of 100 microns per second. Imaging through the fluid rather than in air decreases the protein response by the ratio of $(n_p - n_w)/(n_p - 1) = 0.25$. If the fluid sample is homogeneous and non-turbid, it causes no further degradation in the assay sensitivity, despite the traversal by the probe beam through the fluid. Although the fluid contains unbound target analytes, the differential measurement only detects the incremental mass binding at the surface.

To measure real-time binding, a 20 $\mu\text{g}/\text{mL}$ solution of anti-rabbit in PBS flowed through a well printed with mouse and rabbit IgG in 2×2 unit cells. The measured surface height change as a function of time is plotted in the movie of Fig. 9. In this real-time detection, the disc was not shifted. Instead, the data were taken at different times and were normalized by the first image before the beginning of incubation. The slow temporal variation in the illumination background was removed, to first order, by an interpolation algorithm. The time between each frame in the movie is approximately 40 sec, and the total time is 40 minutes. The entire field of view contains 40 protein spots. The height of the specific spots increases as a function of time. The nonspecific spots remain unchanged and hence are not detectable in the movie of Fig. 9.

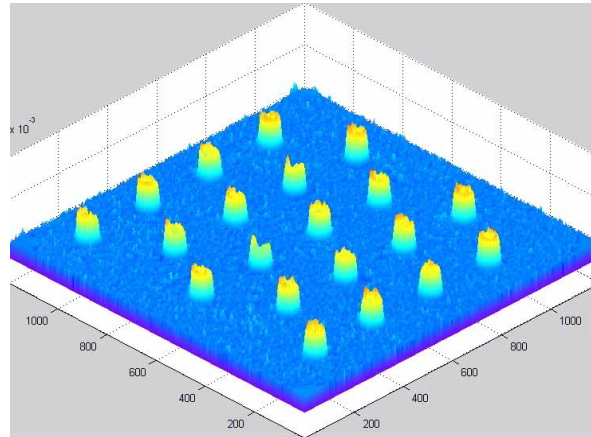


Fig. 9. Movie of real-time binding of anti-rabbit at 20 $\mu\text{g}/\text{ml}$ against spotted rabbit IgG. File size 2.80 MB

Real-time kinetic curves for 5 different concentrations ranging from 2 $\mu\text{g}/\text{ml}$ to 40 $\mu\text{g}/\text{ml}$ are shown in Fig. 10(a). In Fig. 10(b), the same data are plotted on a horizontal axis that is rescaled as the concentration-time product. The data at different concentrations collapse onto a common curve at low binding values, while asymptoting to different saturated values at large binding values. The knee for the kinetic curves occurs at $[C]t = 3 \times 10^4 \mu\text{g sec}/\text{ml}$, which equals a kinetic on rate $K_{on} = 5 \times 10^3 \text{ M}^{-1}\text{sec}^{-1}$. The data for the lowest concentrations and times run into the noise floor at 2 pm average protein spot height change, which leads to a dynamic range of 10^3 for surface height, and over 10^2 for the concentration-time product.

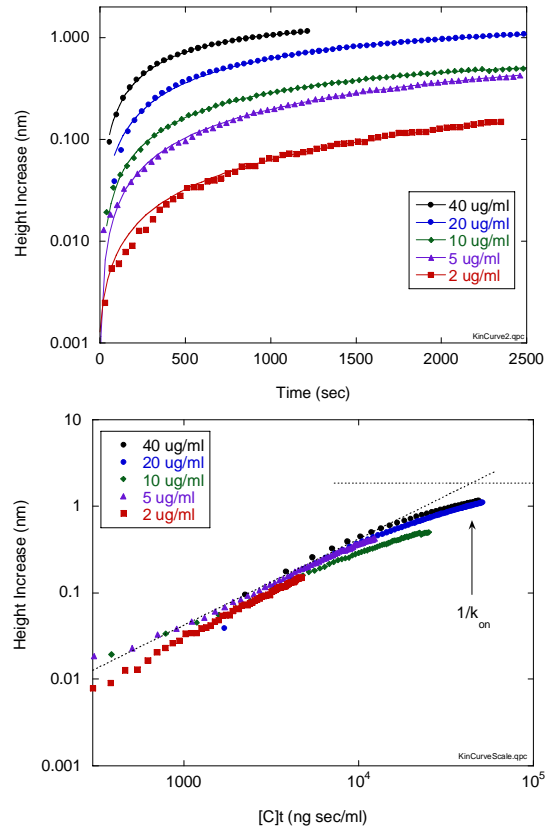


Fig. 10. (a) Kinetic binding of anti-rabbit against rabbit plotted as the average spot height increase versus incubation time. (b) The horizontal axis is rescaled by $[C]t$ to collapse the data. The knee of the kinetic curves occurs at 3×10^4 mg sec/ml. The kinetic on rate K_{on} is determined to be 5×10^3 M⁻¹sec⁻¹.

The dissociation of IgG from the fusion protein A/G as a function of buffer pH was studied by real-time imaging under 7x magnification, as shown in Fig. 11. A 96-well disc was printed with protein A/G, and several wells on the disc were used for the real-time binding experiment. PBS buffer with 0.05% Tween 20 was first flowed through the flow cell, which set the baseline of the measurements. Then 10 μ g/mL of rabbit IgG in PBS buffer was flowed across the protein A/G spots at a volume rate of 0.5 mL/hour. The rabbit IgG was captured onto the protein A/G spots, which increased about 2 nm in height. Solutions at different pH values were then flowed through the system, and the dissociation of rabbit IgG was measured. With decreasing pH, the dissociation rate increases dramatically. For this experiment we did not regenerate the protein A/G spots, but used separate wells for each concentration.

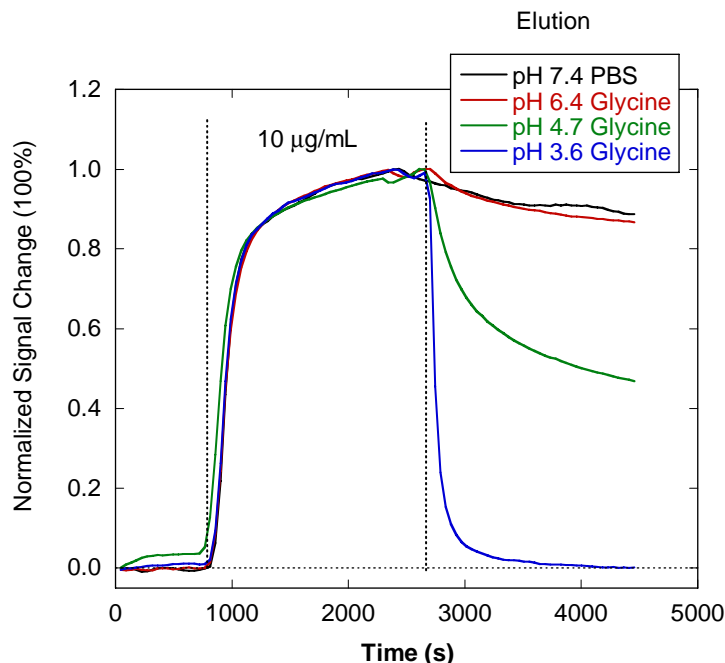


Fig. 11. Real-time binding of 10 µg/ml antibody to the fusion protein A/G, followed by elution at decreasing pH. The standard error of the measurements is at 3 pm averaged over 32 spots.

The detection sensitivity for real-time binding is different than the static detection assay because the variation in the illumination field F_{ij} is removed by temporal shift instead of spatial shift. The data acquired at different times were referenced against the data collected at a previous time to obtain $D_{ij;\Delta t}$

$$D_{ij;\Delta t} = 2 \frac{I_{ij;t+\Delta t} - I_{ij;t}}{I_{ij;t+\Delta t} + I_{ij;t}} \approx C(\lambda, d)(h_{ij;t+\Delta t} - h_{ij;t}) \quad (10)$$

Because no spatial shift is required, the detection is not limited by surface roughness, but rather by long-term system drift, which is the temporal component of F_{ij} . Also, because the detection is performed under water, $C(\lambda, d)$ is reduced by four times because of the lower refractive index contrast between protein and the water medium. Real-time binding removes the need for off-line chemistry and disc dry-down, thus reducing error caused by chemical processing. The standard error in the real-time binding curve under 7x magnification is 3 pm when averaged over 32 protein spots with $N = 128$, which is converted to a mass sensitivity of 2 pg/mm² by Eq. (8).

8. Conclusion

In this letter we have demonstrated the high surface mass sensitivity of molecular interferometric imaging when used in surface metrology applications, with a scaling mass sensitivity of 7 fg/mm, limited by surface roughness of the reference land adjacent to protein spots. The approach is simple and inexpensive, and uses well-established microscopy techniques for illumination normalization. The combination of in-line quadrature with shearing interferometry and the application to measuring molecular layers on surfaces is new. The molecular sensitivity approaches single-molecule detection levels without fluorescent tags or other labels. We have demonstrated practical immunoassays, showing concentration sensitivity of 10 ng/ml in the presence of high protein background concentration. The utility

of molecular interferometric imaging for real-time kinetic experiments was demonstrated with performance of 2 pg/mm^2 comparable to surface plasmon resonance sensors. The high sensitivity and easy multiplexing of the technique make it promising for surface metrology and future medical molecular diagnostics.

Acknowledgment:

This work was supported by sponsored research from Quadraspec, Inc. through the Purdue Research Foundation.